Active foam dynamics of tissue spheroid fusion

Steven Ongenae[1,2], Hanna Svitina[2,3], Tom E. R. Belpaire[1], Jef Vangheel[1], Tobie Martens[4], Pieter Vanden Berghe[4], Ioannis Papantoniou[2,3], and Bart Smeets[1,2]

[1]MeBioS, Department of Biosystems, KU Leuven, Leuven, Belgium
[2]Prometheus, Division of Skeletal Tissue Engineering, KU Leuven, Leuven, Belgium
[3]Skeletal Biology and Engineering Research Center, Department of Development and Regeneration, KU Leuven, Leuven, Belgium
[4]Cell & tissue Imaging Core, KU Leuven, Leuven, Belgium

Supplementary Information

Supplementary Note: Alternative visco-elastic model for spheroid fusion

The visco-elastic model for tissue spheroid fusion used in this work (see main paper, Eq. 2) assumes that both viscous dissipation and elastic deformation occur uniformly throughout the bulk spheroid. In making these assumptions, it is highly similar to work by Oriola et al. [1] (similarities and differences are discussed in [2]).

However, alternatively, one can assume that elastic deformation and viscous dissipation are more local in the contact region, and that they occur within a region whose volume scales as a^3, where a is the contact radius. These assumptions are motivated by the observation that the radius of a spreading aggregate [3] and the contact radius of two fusing spheroids [4] scale $\propto t^{1/3}$. Based on the Michel and Shanahan model [5], a viscoelastic extension JKR theory, Beaune et al. a viscoelastic liquid fusion model. The rheological representation of this model is of a Kelvin-Voigt model in series with a viscous damper, to account for liquid-like flow at long timescales. Under the assumption that aggregate indentation is governed by JKR theory, this leads to a proposed scaling of the contact radius in time, with aggregate radius R,

$$\frac{a^3}{R^2} \approx L_e \left(1 - e^{-\frac{t}{\tau_1}}\right) + v_f t. \tag{S1}$$

Here, $L_e \propto \Gamma/E \propto \Gamma/G'$ is an elastic length-scale, with aggregate surface tension Γ, Young's modulus E and shear modulus G'. L_e represents the extent of elastic deformation induced by the driving force of surface tension, and a higher value of L_e thus corresponds to a softer, less elastic tissue. Further, τ_1 is the initial visco-elastic relaxation time of the Michel and Shanahan model of visco-elastic adhesion. It corresponds to the exponential relaxation time of the initial visco-elastic response. Finally, $v_f \propto \Gamma/\eta_t$ is the long-timescale characteristic fusion velocity, with effective tissue viscosity η_t. Given its reliance on JKR theory, this model is expected to hold for relatively small deformations. Clearly, this assumption is violated near full fusion. We fitted this model to our experimental data using the same procedure as for our primary model. The resulting fits are shown in Supplementary Fig. 3 and the fitted parameters L_e, τ_1 and v_f are shown in Supplementary Fig. 4.

Supplementary Methods: Deformable Cell Model

In this supplementary note, we present the details of the deformable cell model, which is akin to the work of Cuvelier et al. [6], where viscous cells are modeled using a particle-based representation. The tissue is treated as an active foam where each cell behaves as a pressurized "bubble" with surface tension, adhesion, and internal pressure. The acto-myosin cortex of a cell is modeled as a viscous, tensed shell, approximated by a triangulated surface mesh with effective thickness t, and nodal positions $\boldsymbol{x}_i$ as the primary (translational) degrees of freedom. Forces acting on the nodes are categorized into three distinct types based on their origin. The subsequent sections will discuss the different force contributions and their implementation.

Surface tension

Tension generated in the cortex results from acto-myosin contractility, which is represented as the effective free-surface tension γ in the shell model. Moreover, the in-plane contribution of interfacial adhesion energy w generates a negative surface tension in contacting surfaces. Hence, the net surface tension γ_s on a given surface element is

$$\gamma_s = \begin{cases} \gamma - \frac{w}{2}, & \text{for contacting surfaces and,} \\ \gamma & \text{for free surfaces.} \end{cases} \tag{S2}$$

The factor $1/2$ for the adhesion energy is included because in our model w represents the 'net work of adhesion' between two contacting surfaces. It should be noted that, in our model, there is no fundamental difference between adhesion and (reduction in) interfacial tension. Hence, while the underlying physical mechanism that governs contact angles in biological systems is a reduction in contractility [7], the net physical effect is an adhesive tension. Both the effects of adhesion and reduced interfacial tension are captured in the relative cell-cell tension,

$$\alpha = 1 - \frac{w}{\gamma}, \tag{S3}$$

which uniquely parameterizes the contact angle θ_c between two adjacent cells, $\cos(\theta_c) = \alpha$. Using the derivation of Fedosov et al. [8], the direct force contribution of surface tension γ_s of node i is given by

$$\boldsymbol{F}_i^{\text{act}} = \frac{\gamma_s}{2}(\boldsymbol{x}_k - \boldsymbol{x}_j) \times \hat{\boldsymbol{n}}_A, \tag{S4}$$

where i, j, k are nodes of a single triangle $A = (ijk)$.

Internal pressure

Since the cytoplasm is assumed to be incompressible, active volume control is implemented via a cytoplasmic pressure. We assume the equilibrium volume V_l^* of a cell l is constant and implemented a proportional-integral (PI) pressure controller to enforce this. The cytoplasmic pressure $P_l^{\text{cyt}}(t)$ due to the volume controller is then

$$P_l^{\text{cyt}}(t) = -K\varepsilon_l(t) - \frac{K}{\tau_K}\int_0^t \mathrm{d}s\, \varepsilon_l(s), \tag{S5}$$

for a cell with volumetric strain $\varepsilon_l(t) = (V_l(t) - V_l^*)/V_l^*$. The total pressure acting on a cell

$$P_l(t) = \frac{2\gamma}{r_l} + P_l^{\text{cyt}}(t), \tag{S6}$$

includes an additional offset pressure $2\gamma/r_l$ to balance the acto-myosin contractility in the cortex. This ensures cells are in mechanical equilibrium at the start of the simulations. The force acting on triangle A due to internal pressure $P_l(t)$, is obtained by multiplying with the triangle area vector $\boldsymbol{S_A} = S_A\hat{\boldsymbol{n}}_A$. Given the pressure is constant over the triangle surface, the force per triangle is

$$\boldsymbol{F}_A^{\text{cyt}}(t) = \boldsymbol{S}_A P_l(t). \tag{S7}$$

These volume forces are then equally distributed to the nodes (ijk).

Cell migration

Cell migration is modeled as a protrusive pressure at the leading cell edge and a contractile pressure at the trailing edge, resembling mesenchymal migration by actomyosin polymerisation and cell contraction, respectively. The pressure on node i in cell l is modeled as

$$P_i^a = p_a \frac{S_{c,l}}{S_l} \frac{\boldsymbol{x}_i - \boldsymbol{x}_{c,l}}{||\boldsymbol{x}_i - \boldsymbol{x}_{c,l}||} \cdot \hat{\boldsymbol{p}}_l \tag{S8}$$

where p_a is the active pressure, $S_{c,l}$ is the cell-cell contact area of cell l and S_l is the total cell area, $x_{c,l}$ is cell center and $\hat{\boldsymbol{p}}_l$ is the cell polarity. The active force on node i is

$$\boldsymbol{F}_i^{\text{act}} = p_i^a \hat{\boldsymbol{n}}_i. \tag{S9}$$

We assume that the polarity $\hat{\boldsymbol{p}}_l$ undergoes rotational diffusion

$$\mathrm{d}\hat{\boldsymbol{p}}_l = \sqrt{2D_r}\,\mathrm{d}\boldsymbol{W}_{t,l} \times \hat{\boldsymbol{p}}_l \tag{S10}$$

with persistence time $\tau_p = 1/D_r$ and standard Wiener process $\boldsymbol{W}_{t,l}$ [9]. The internal force balance is preserved by distributing a reaction traction force over the cell contact area

$$\boldsymbol{F}_i^{\text{react}} = \begin{cases} -\frac{S_i}{S_{c,l}} \sum_{j \in l} P_j^a S_j \hat{\boldsymbol{n}}_j & \text{for contacting surfaces and,} \\ \boldsymbol{0} & \text{else.} \end{cases} \tag{S11}$$

This guarantees that $\sum_i \boldsymbol{F}_i^{\text{act}} + \boldsymbol{F}_i^{\text{react}} = \boldsymbol{0}$, ensuring conservation of internal momentum.

Medium damping

Medium drag is included as

$$\boldsymbol{F}_i^{\text{drag}} = -\boldsymbol{\Gamma}_{ii}^m \boldsymbol{v}_i,$$

where

$$\boldsymbol{\Gamma}_{ii}^m = \frac{3\eta_m}{2r} S_i \boldsymbol{I}, \tag{S12}$$

with apparent medium viscosity η_m. While η_m could be interpreted as the viscosity of the cell surrounding (i.e., water), this contribution is negligible compared to the long-time viscous behavior of multicellular systems. Hence, η_m should be interpreted as an artificial medium damping that is included to improve the numerical stability of the integration scheme [10]. In this work, η_m is chosen to be much lower than other relevant viscosities in the system to ensure that the precise value of η_m does not affect the outcome of the simulations.

Cortex viscosity

Planar extensional viscosity

A significant contribution to energy dissipation arises from 2D cortex viscosity (units of N·s/m), which we assume arises at long timescales due to remodeling of the acto-myosin cortex [11]. The viscous damping force between two connected nodes of the triangular mesh is given by

$$\boldsymbol{F}_{ij}^{\text{visc}} = \boldsymbol{\Gamma}_{ij}^c((\hat{\boldsymbol{n}}_{ij} \cdot (\boldsymbol{v}_j - \boldsymbol{v}_i))\hat{\boldsymbol{n}}_{ij} + (\hat{\boldsymbol{t}}_{ij} \cdot (\boldsymbol{v}_j - \boldsymbol{v}_i))\hat{\boldsymbol{t}}_{ij}) + \varepsilon_n(\hat{\boldsymbol{b}}_{ij} \cdot (\boldsymbol{v}_j - \boldsymbol{v}_i))\hat{\boldsymbol{b}}_{ij})), \tag{S13}$$

with friction element

$$\boldsymbol{\Gamma}_{ij}^{\text{c}} = \frac{\eta}{\sqrt{3}},$$

and unit vectors

$$\hat{\boldsymbol{n}}_{ij} = \frac{\boldsymbol{x}_j - \boldsymbol{x}_i}{\|\boldsymbol{x}_j - \boldsymbol{x}_i\|},$$

$$\hat{\boldsymbol{b}}_{ij} = \frac{\hat{\boldsymbol{n}}_A + \hat{\boldsymbol{n}}_B}{\|\hat{\boldsymbol{n}}_A + \hat{\boldsymbol{n}}_B\|},$$

$$\hat{\boldsymbol{t}}_{ij} = \hat{\boldsymbol{b}}_{ij} \times \hat{\boldsymbol{n}}_{ij},$$

with $\hat{\boldsymbol{n}}_A$, and $\hat{\boldsymbol{n}}_B$, the normal unit vectors of the triangles making up the segment between nodes i and j. We further set $\varepsilon_n = 1/10$ as a "numerically small" out-of-plane shear viscosity to prevent spurious out-of-plane numerical oscillations. This introduces artificial bending viscosity in the model, which is sufficiently low to not affect the results of our simulations [6].

Wet contact friction

A viscous contact force is included to account for drag between contacting surfaces with friction constant ξ (units of Pa·s/m), expressing the scaling between dissipative traction and the sliding velocity of two contacting surfaces A and B

$$\boldsymbol{T}_{AB}^{\text{fric}} = -\xi \Delta \boldsymbol{v}_{AB}. \tag{S14}$$

In the particle-based model, the contact drag force acting on node i of triangle A of the contact pair (AB) is computed as

$$\boldsymbol{F}_{AB,i}^{\text{fric}} = \boldsymbol{\Gamma}_{AB}^{\text{fric}} \cdot \sum_{k \in B} w_{ik}^{AB} \, (\boldsymbol{v}_k - \boldsymbol{v}_i) \tag{S15}$$

determined by a friction tensor $\boldsymbol{\Gamma}_{AB}^{\text{fric}}$ and weights w_{ik}^{AB} per node k of the B triangle. w_{ik}^{AB} are assumed to scale with the relative contribution of the nodal contact forces to the overall contact force thus

$$w_{ik}^{AB} = \frac{\left(\boldsymbol{F}_{AB,i}^{\text{adh}} + \boldsymbol{F}_{AB,k}^{\text{adh}}\right) \cdot \hat{\boldsymbol{n}}_{AB}}{6 \sum\limits_{\forall k \in B} \boldsymbol{F}_{AB,k}^{\text{adh}} \cdot \hat{\boldsymbol{n}}_{AB}}$$

is used as an approximation. $\boldsymbol{\Gamma}_{AB}^{\text{fric}}$ for a given contact area S_{AB} is estimated as

$$\boldsymbol{\Gamma}_{AB}^{\text{fric}} = S_{AB} \left[\xi^{\perp} \hat{\boldsymbol{n}}_{AB} \otimes \hat{\boldsymbol{n}}_{AB} + \xi^{\parallel} \left(\boldsymbol{I} - \hat{\boldsymbol{n}}_{AB} \otimes \hat{\boldsymbol{n}}_{AB} \right) \right],$$

with normal and tangential friction coefficients $\xi^{\perp}$ and $\xi^{\parallel}$ respectively. Note that Eq. (S15) can be equivalently formulated as

$$\boldsymbol{F}_{AB,i}^{\text{fric}} = \sum_{k \in B} \boldsymbol{\Gamma}_{AB,ik}^{\text{fric}} \cdot (\boldsymbol{v}_k - \boldsymbol{v}_i),$$

if we denote

$$\boldsymbol{\Gamma}_{AB,ik}^{\text{fric}} = w_{ik}^{AB} \boldsymbol{\Gamma}_{AB}^{\text{fric}}. \tag{S16}$$

Contact forces

In the mechanical cell model, we assume a fixed and uniform adhesive tension w across the cell surface. The adhesive tension incorporates cell-cell adhesive interactions as well as the effect of cortical tension reduction at the cell-cell interface [7, 12, 13]. The total adhesive tension w acting on interface (AB) is given by $w = w_A + w_B$. A linear force,

scaling with contact overlap δ, was introduced to represent repulsive interactions between surfaces and ensure stable contacts. The contact potential for contact-pair (AB) with contact area S_{AB} is then given by

$$E_{AB}^{\text{adh}} = \left(\frac{\delta_{AB}}{h_0} - \frac{\delta_{AB}^2}{2h_0^2} \right) w S_{AB}$$

where a distinction can be made between the attractive and repulsive energy contributions respectively. The effective range of adhesion h_0 was incorporated by virtually translating contact surfaces along their normal direction. The contact overlap distance δ_{AB} is calculated with respect to these translated surfaces. The resulting contact pressure P_{AB}^{adh} is estimated with a linear contact pressure model where no energy is stored in deformation at equilibrium

$$P_{AB}^{\text{adh}}(\boldsymbol{x}) = k_{AB}\delta_{AB}(\boldsymbol{x}) - P_{AB}^0,$$

contact stiffness k_{AB} and adhesive pressure P_{AB}^0 need to be set. To ensure that at equilibrium ($P_{AB}^{\text{adh}} \equiv 0$) the work of adhesion w is recovered, contact stiffness has to be defined as $k_{AB} = P_{AB}^0/h_0$ with $P_{AB}^0 = w/h_0$. In contrast to previous work [6], it was opted to keep k_{AB} constant because at low adhesion the contact between cells was insufficiently stiff leading to cells collapsing in each other. We set k_{AB} based on a middle adhesion level at reference surface tension γ_{ref} (see Table 1), $w_A = w_B = 0.4\gamma_{ref}$, and a reference effective range $h_{0,\text{ref}}$ =75 nm, hence $k_{AB} \approx 711$ kPa/nm. This implies that the effective range changes when varying adhesion i.e. $h_0 = \sqrt{w/k_{AB}}$. Nevertheless, the specific value h_0 does not influence simulation outcome due to the scale separation, $h_0 \ll R^{\text{cell}}$. The contact overlap distance at point $\boldsymbol{x}$ is obtained as

$$\delta_{AB}(\boldsymbol{x}) = \max\left\{0;\ 2(\boldsymbol{x} - \boldsymbol{s}_{AB}) \cdot \left(\hat{\boldsymbol{n}}_{AB} \times \hat{\boldsymbol{l}}_{AB}\right) \tan\theta\right\},$$

where θ is the contact angle, $\hat{\boldsymbol{n}}_{AB} \propto (\hat{\boldsymbol{n}}_B - \hat{\boldsymbol{n}}_A) \times \hat{\boldsymbol{l}}_{AB}$ the contact normal and $\boldsymbol{s}_{AB}$ is an arbitrary point on the intersection line defined by $\hat{\boldsymbol{l}}_{AB} \propto \hat{\boldsymbol{n}}_A \times \hat{\boldsymbol{n}}_B$, as reported by Smeets et al. [14]. The resulting contact forces and moment are obtained by integrating the total contact pressure over the oriented contact area $\boldsymbol{S}_{AB}$,

$$\boldsymbol{F}_{AB}^{\text{adh}} = \int \mathrm{d}\boldsymbol{S}_{AB}(\boldsymbol{x})\, P_{AB}^{\text{adh}}(\boldsymbol{x}). \tag{S17}$$

To distribute the contact forces acting on the contact plains to the nodal contact forces $\boldsymbol{F}_{AB,i}^{\text{adh}}$, it is assumed that the nodal forces are collinear with the contact normal $\hat{\boldsymbol{n}}_{AB}$. This results in a system of linear equations per contact pair (AB)

$$\begin{aligned} \sum_{i\in A} \boldsymbol{F}_{AB,i}^{\text{adh}} &= -\int_{\boldsymbol{x}\in A\cap B} \mathrm{d}\boldsymbol{S}_{AB}(\boldsymbol{x})\, P_{AB}^{\text{adh}}(\boldsymbol{x}) \\ \sum_{i\in A} \left[(\boldsymbol{I} - \hat{\boldsymbol{n}}_{AB} \otimes \hat{\boldsymbol{n}}_{AB}) \cdot (\boldsymbol{x}_i - \boldsymbol{x}_{AB})\right] \times \boldsymbol{F}_{AB,i}^{\text{adh}} &= \int_{\boldsymbol{x}\in A\cap B} \mathrm{d}\boldsymbol{S}_{AB}(\boldsymbol{x}) \times (\boldsymbol{x} - \boldsymbol{x}_{AB})\, P_{AB}^{\text{adh}}(\boldsymbol{x}) \end{aligned} \tag{S18}$$

which guarantees a unique solution for every $\boldsymbol{F}_{AB,i}^{\text{adh}}$. The contact point $\boldsymbol{x}_{AB}$ is defined as the geometric center of the intersection polygon $A \cap B$. [14] The integrals on the right hand side are calculated by using a numerical quadrature rule presented in [15] with 7 quadrature points covering each triangle of the triangulated intersection polygon $A \cap B$ obtained as an intersection of projected triangles on a common plane. The precise choice of the number of quadrature points has no impact on the results in the simulation, as long as adequate quadrature coordinates and weighting values are chosen. The solution for this system is presented and discussed in the work of Smeets et al. [14].

Equation of motion

In the overdamped cellular environment, inertial forces may be neglected. Based on the different contributions described above, the force balance for node i gives

$$\boldsymbol{F}_i^{\text{act}} + \boldsymbol{F}_i^{\text{react}} + \boldsymbol{F}_i^{\text{cyt}} + \sum_{(AB):i\in A} \boldsymbol{F}_{AB,i}^{\text{adh}} = \Gamma_{mii}\cdot\boldsymbol{v}_i + \sum_j \boldsymbol{\Gamma}_{ij}^{\text{c}}\cdot(\boldsymbol{v}_i - \boldsymbol{v}_j) + \sum_{(AB):i\in A}\sum_{k\in B} \boldsymbol{\Gamma}_{AB,ik}^{\text{fric}}\cdot(\boldsymbol{v}_i - \boldsymbol{v}_k)$$

which can be abbreviated as

$$\boldsymbol{F}_i = \sum_j \boldsymbol{\Gamma}_{ij}\cdot\boldsymbol{v}_j \tag{S19}$$

for a system consisting of N nodes, where

$$\boldsymbol{\Gamma}_{ij} = \begin{cases} \boldsymbol{\Gamma}_{ii}^{m} + \sum\limits_{k:k\neq i} \boldsymbol{\Gamma}_{ik}^{\text{c}} + \sum\limits_{(AB):i\in A}\sum\limits_{k\in B} \boldsymbol{\Gamma}_{AB,ik}^{\text{fric}}, & i = j, \\ -\boldsymbol{\Gamma}_{ij}^{\text{c}} - \sum\limits_{(AB):i\in A, j\in B} \boldsymbol{\Gamma}_{AB,ij}^{\text{fric}}, & i \neq j. \end{cases}$$

The Cartesian components of the overall force vectors can be represented as a single $(3N\times 1)$ column matrix, $\mathbf{F} = [\boldsymbol{F}_1,\ldots,\boldsymbol{F}_i,\ldots,\boldsymbol{F}_n]^T$, while the friction matrices can be assembled to a single $(3N\times 3N)$ sparse symmetric positive definite friction matrix $\boldsymbol{\Gamma}$ [16], hence obtaining the linear system

$$\boldsymbol{\Gamma}\,\mathbf{v} = \mathbf{F}. \tag{S20}$$

The conjugate gradient method (CGM) is used to efficiently solve this system for the node velocities $\mathbf{v}(t+\Delta t)$ at each iteration in a semi-implicit scheme. Positions of the nodes are subsequently updated using backward Euler integration,

$$\mathbf{x}(t+\Delta t) = \mathbf{x}(t) + \Delta t\,\mathbf{v}(t+\Delta t), \tag{S21}$$

where $\mathbf{v}(t+\Delta t)$ are the projected new velocities obtained by solving Eq. S20 at time t via the CGM.

Remeshing

Due to the viscous material properties of the cortex, mesh nodes tend to flow as no local area or length conservation is imposed. To maintain a mesh of sufficiently high quality, i.e. sufficiently high resolution near fine details of the cell at an acceptable number of degrees of freedom, we used a remeshing algorithm based on the surface operations defined by Brakke [17] using as input a threshold minimum and maximum triangle area, similar to [18]. The remeshing step is performed every 30 time steps to ensure a sufficiently high mesh quality. By remeshing, we implicitly assume that the nodes themselves do not carry 'mass' or other local information, but are merely considered as discretization points that represent the location of the surface. Similarly, there can be no conservative (energy conserving) potentials in the membrane, since no history of previous deformation is retained in the computational model [19]. However, these conditions are explicitly assumed by the viscous approximation of the cortex model.

Model parameters

Table 1 provides a list of all parameter used to simulate tissue spheroid fusion with the active foam model. The table is divided into three categories: 1) Model parameters which are constant over all performed simulations; 2) Model parameters which can vary in between simulations of a parameter study. Unless mentioned otherwise, these are the parameters used in the reported results; 3) Simulation parameter, which are associated to the numerical solutions of the simulation. Only dimensions of length and time were accessible in experiments. Furthermore, no absolute sizes, but fusion angles were reported. Hence all simulation results are reported in reduced model parameters, which are adimensional or only contain units of time. These reduced parameters are provided in Table 2.

References

[1] David Oriola, Miquel Marin-Riera, Kerim Anlaş, Nicola Gritti, Marina Sanaki-Matsumiya, Germaine Aalderink, Miki Ebisuya, James Sharpe, and Vikas Trivedi. Arrested coalescence of multicellular aggregates. *Soft Matter*, 18(19):3771–3780, 2022.

[2] Steven Ongenae, Maxim Cuvelier, Jef Vangheel, Herman Ramon, and Bart Smeets. Activity-induced fluidization and arrested coalescence in fusion of cellular aggregates. *Frontiers in Physics*, 9:649821, 2021.

[3] Stéphane Douezan, Karine Guevorkian, Randa Naouar, Sylvie Dufour, Damien Cuvelier, and Françoise Brochard-Wyart. Spreading dynamics and wetting transition of cellular aggregates. *Proceedings of the National Academy of Sciences*, 108(18):7315–7320, 2011.

[4] Grégory Beaune, Laura Sinkkonen, David Gonzalez-Rodriguez, Jaakko VI Timonen, and Françoise Brochard-Wyart. Fusion dynamics of hybrid cell–microparticle aggregates: A jelly pearl model. *Langmuir*, 38(17):5296–5306, 2022.

[5] F Michel and MER Shanahan. Kinetics of the jkr experiment. *CR Acad. Sci. II*, 310:17–20, 1990.

[6] Maxim Cuvelier, Jef Vangheel, Wim Thiels, Herman Ramon, Rob Jelier, and Bart Smeets. Stability of asymmetric cell division: A deformable cell model of cytokinesis applied to c. elegans. *Biophysical Journal*, 122(10):1858–1867, 2023.

[7] Jean-Léon Maître, Hélène Berthoumieux, Simon Frederik Gabriel Krens, Guillaume Salbreux, Frank Jülicher, Ewa Paluch, and Carl-Philipp Heisenberg. Adhesion functions in cell sorting by mechanically coupling the cortices of adhering cells. *Science*, 338:253–256, 2012.

[8] D. Fedosov, B. Caswell, and G. Karniadakis. Systematic coarse-graining of spectrin-level red blood cell models. *Comput. Methods Appl. Mech. Eng.*, 199:29–32, 2010.

[9] Joakim Stenhammar, Davide Marenduzzo, Rosalind J Allen, and Michael E Cates. Phase behaviour of active brownian particles: the role of dimensionality. *Soft matter*, 10(10):1489–1499, 2014.

[10] Paul Van Liedekerke, Bart Smeets, Tim Odenthal, Engelbert Tijskens, and Herman Ramon. Solving microscopic flow problems using stokes equations in sph. *Comput. Phys. Commun.*, 184:1686–1696, 2013.

[11] Arnab Saha, Masatoshi Nishikawa, Martin Behrndt, Carl-Philipp Heisenberg, Frank Jülicher, and Stephan W Grill. Determining physical properties of the cell cortex. *Biophys. J.*, 110(6):1421–1429, 2016.

[12] Hervé Turlier and Jean-Léon Maître. Mechanics of tissue compaction. *Semin. Cell Dev. Biol.*, 47-48:110–117, 2015.

[13] Carl-Philipp Heisenberg and Yohanns Bellaïche. Forces in tissue morphogenesis and patterning. *Cell*, 153:948–962, 2013.

[14] Bart Smeets, Tim Odenthal, Simon Vanmaercke, and Herman Ramon. Polygon-based contact description for modeling arbitrary polyhedra in the discrete element method. *Comput. Methods Appl. Mech. Eng.*, 290:277–289, 2015.

[15] Linbo Zhang, Tao Cui, and Hui Liu. A set of symmetric quadrature rules on triangles and tetrahedra. *J. Comput. Math*, 27:89–96, 2009.

[16] Tim Odenthal, Bart Smeets, Paul Van Liedekerke, Engelbert Tijskens, Hans Van Oosterwyck, and Herman Ramon. Analysis of initial cell spreading using mechanistic contact formulations for a deformable cell model. *PLoS Comput. Biol.*, 9:e1003267, 2013.

[17] Kenneth A Brakke. The surface evolver. *Exp. Math.*, 1:141–165, 1992.

[18] Steve Runser, Roman Vetter, and Dagmar Iber. Simucell3d: three-dimensional simulation of tissue mechanics with cell polarization. *Nature Computational Science*, pages 1–11, 2024.

[19] Bart Smeets, Maxim Cuvelier, Jiri Pešek, and Herman Ramon. The effect of cortical elasticity and active tension on cell adhesion mechanics. *Biophys. J.*, 116:930–937, 2019.

Supplementary Table 1: **Reference table of model parameters**

Parameter	Symbol	Value	Units
Constants Deformable Cell Model			
Mean cell radius	r	8.88	µm
Cell radius Gamma distribution k-parameter		37	–
Cell radius Gamma distribution theta-parameter		0.24	µm
Contact stiffness	k_{AB}	711.11...	$\mathrm{kPa\,nm^{-1}}$
Cortex surface tension reference	γ_{ref}	0.5	$\mathrm{nN\,\mu m^{-1}}$
Effective fluid viscosity	η_m	0.4	kPa s
Effective cortex viscosity	η	0.005	$\mathrm{N\,s\,m^{-1}}$
Characteristic relaxation time of the cell shell	τ_{shell}	$\eta/(2\sqrt{3}\gamma_{\mathrm{ref}})$	s
Cytosolic bulk modulus	K	0.5	kPa
Cytosolic bulk modulus integration timescale	τ_K	$2\tau_{shell}$	s
References for parameter studies			
Number of cells	N	2×100	–
Relative cell-cell tension	α	0.4375	–
Protrusion pressure	p_a	50	Pa
Effective contact friction	ξ	0.25	$\mathrm{kPa\,s\,\mu m^{-1}}$
Cortex surface tension	γ	0.5	$\mathrm{nN\,\mu m^{-1}}$
Cell motility persistence time	τ_p	10	min
Simulation parameters			
Time step	Δt	0.1	s
Remesh interval	τ_r	$5\tau_{shell}$	s
Reference triangle area	A_Δ	$4\pi r^2/320$	$\mu\mathrm{m}^2$
Minimal triangle area	A_m	$A_\Delta/3$	$\mu\mathrm{m}^2$
Maximum triangle area	A_M	$3A_\Delta$	$\mu\mathrm{m}^2$
Eigen conjugate gradient solver tolerance	ε_{CG}	0.001	–

Supplementary Table 2: **Table of reduced model parameters.** Base values of reduced model parameters (adimensional or in units of time). These values are used for all reported results, unless explicitly stated otherwise.

Parameter	Symbol	Value	Units
Cortical relaxation time	$\tau_\gamma = \eta/\gamma$	10	s
Persistence time	τ_p	10	min
Relative active pressure	$p_a r/2\gamma$	0.33	–
Relative cell-cell tension	$\alpha = 1 - w/\gamma$	0.4375	–
Hydrodynamic length	$L_\eta/r = (\eta/\xi)^{1/2}/r$	0.50	–
Number of cells / spheroid	N	100	–

Supplementary Table 3: Different medium composition used in fusion experiments of hPDC tissue spheroids in conditions C8, TGF^{-}, ROCKi^{-} and Bleb/ROCKi^{+}

C8	**TGF^{-}**	**ROCKi^{-}**	**Bleb/ROCKi^{+}**
LG-DMEM (Gibco)	LG-DMEM (Gibco)	LG-DMEM (Gibco)	LG-DMEM (Gibco)
1 mM ascorbate-2 phosphate	1 mM ascorbate-2 phosphate	1 mM ascorbate-2 phosphate	1 mM ascorbate-2 phosphate
100 nM dexamethasone	100 nM dexamethasone	100 nM dexamethasone	100 nM dexamethasone
40 µg/mL proline	40 µg/mL proline	40 µg/mL proline	40 µg/mL proline
20 µM Y-27632	20 µM Y-27632		100 µM Y-27632
1X ITS	1X ITS	1X ITS	1X ITS
100 ng/mL BMP-2	100 ng/mL BMP-2	100 ng/mL BMP-2	100 ng/mL BMP-2
100 ng/mL GDF-5	100 ng/mL GDF-5	100 ng/mL GDF-5	100 ng/mL GDF-5
10 ng/mL TGF-β1		10 ng/mL TGF-β1	10 ng/mL TGF-β1
1 ng/mL BMP-6	1 ng/mL BMP-6	1 ng/mL BMP-6	1 ng/mL BMP-6
0.2 ng/mL FGF-2	0.2 ng/mL FGF-2	0.2 ng/mL FGF-2	0.2 ng/mL FGF-2
			20 µM blebbistatin

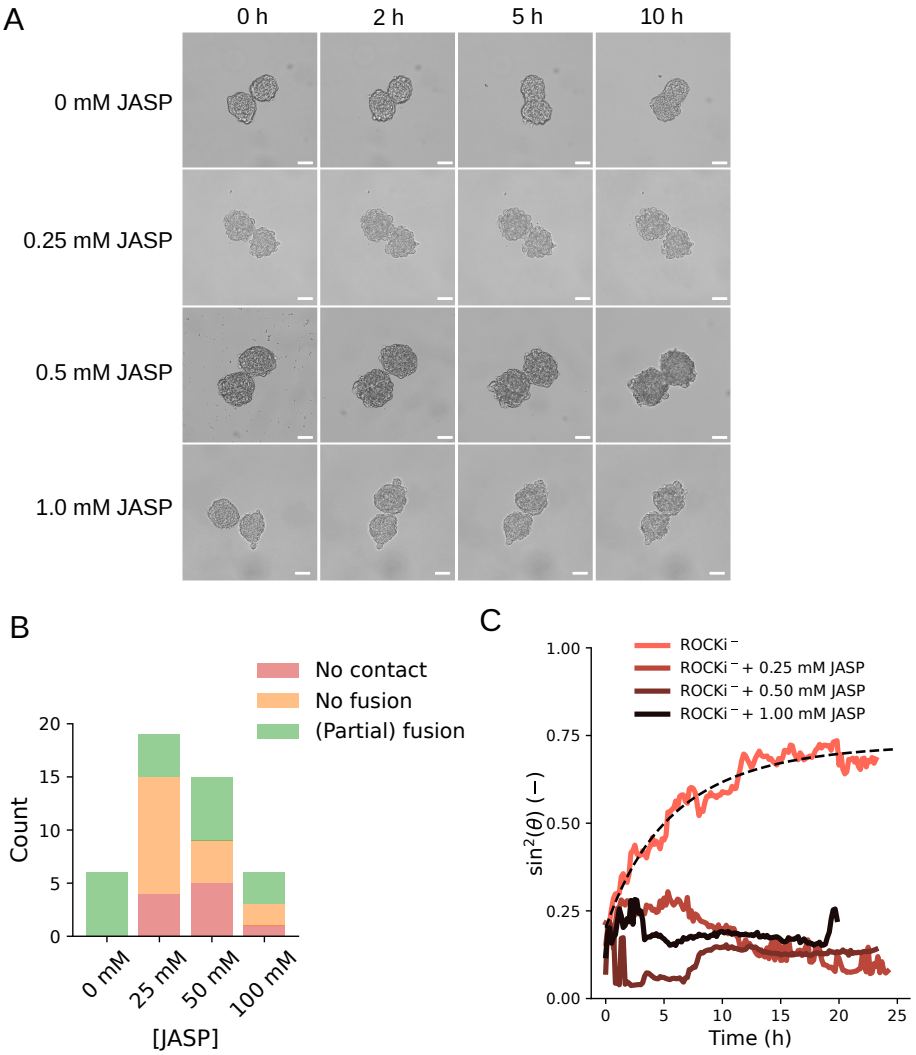

Supplementary Fig. 1: Addition of jasplakinolide (JASP) strongly inhibits spheroid fusion. **A**: Representative time-lapse snapshots of fusion experiments at different levels of JASP at 0, 2, 5 and 10 h. All experiments are performed in ROCK^{-} conditions, to exclude effects of ROCK inhibitor and/or blebbistatin on fusion dynamics. **B**: Characterization of fusion behavior at increasing levels of JASP. No contact: Spheroids were not observed to be in physical contacts. No fusion: Spheroids were in physical contact, but showed no perceivable fusion. (Partial) fusion: Spheroids showed at least partial fusion. Note that in other studied conditions in this work, "No contact" and "No fusion" were absent or rare, and excluded from further analysis. **C**: Fusion angle in function of time for varying concentrations of JASP. Only experiments characterized as "(Partial) fusion" in **(B)** were retained for this analysis.

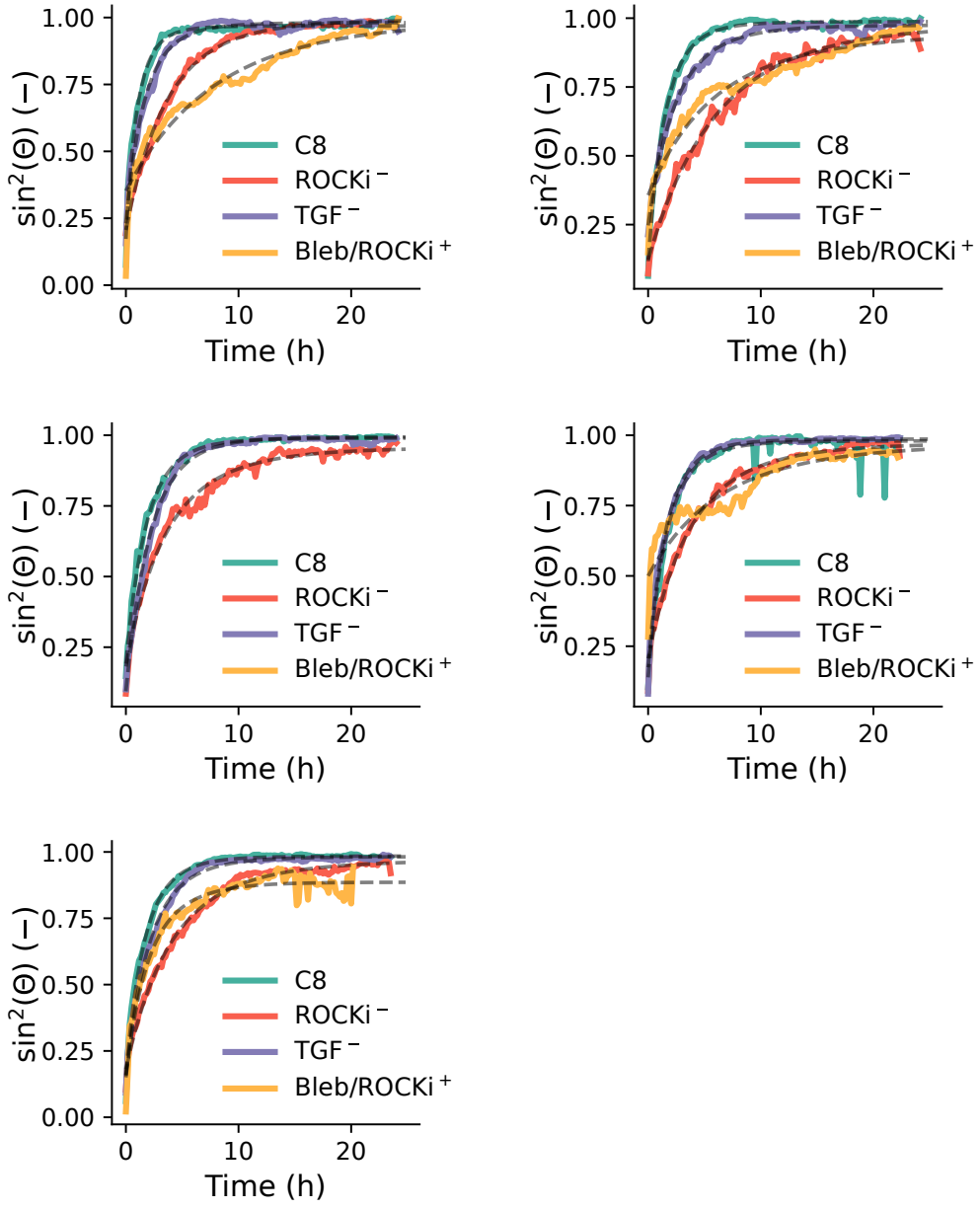

Supplementary Fig. 2: Temporal evolution of the average fusion angle for 4 medium compositions, together with the fit of the governing dynamics $2\dot{\theta} = \cot(\theta)/\tau_\Gamma - \sin(\theta)/\tau_\varepsilon$. Data acquired on the same day is shown in each subplot. Number of studied doublets (n) for each of the five independent biological repeats: C8: 7, 6, 5, 5, 15; ROCKi$^-$: 10, 5, 5, 10, 16; TGF$^-$: 8, 7, 9, 9, 11; Bleb/ROCKi$^+$: 9, 5, –, 3, 5.

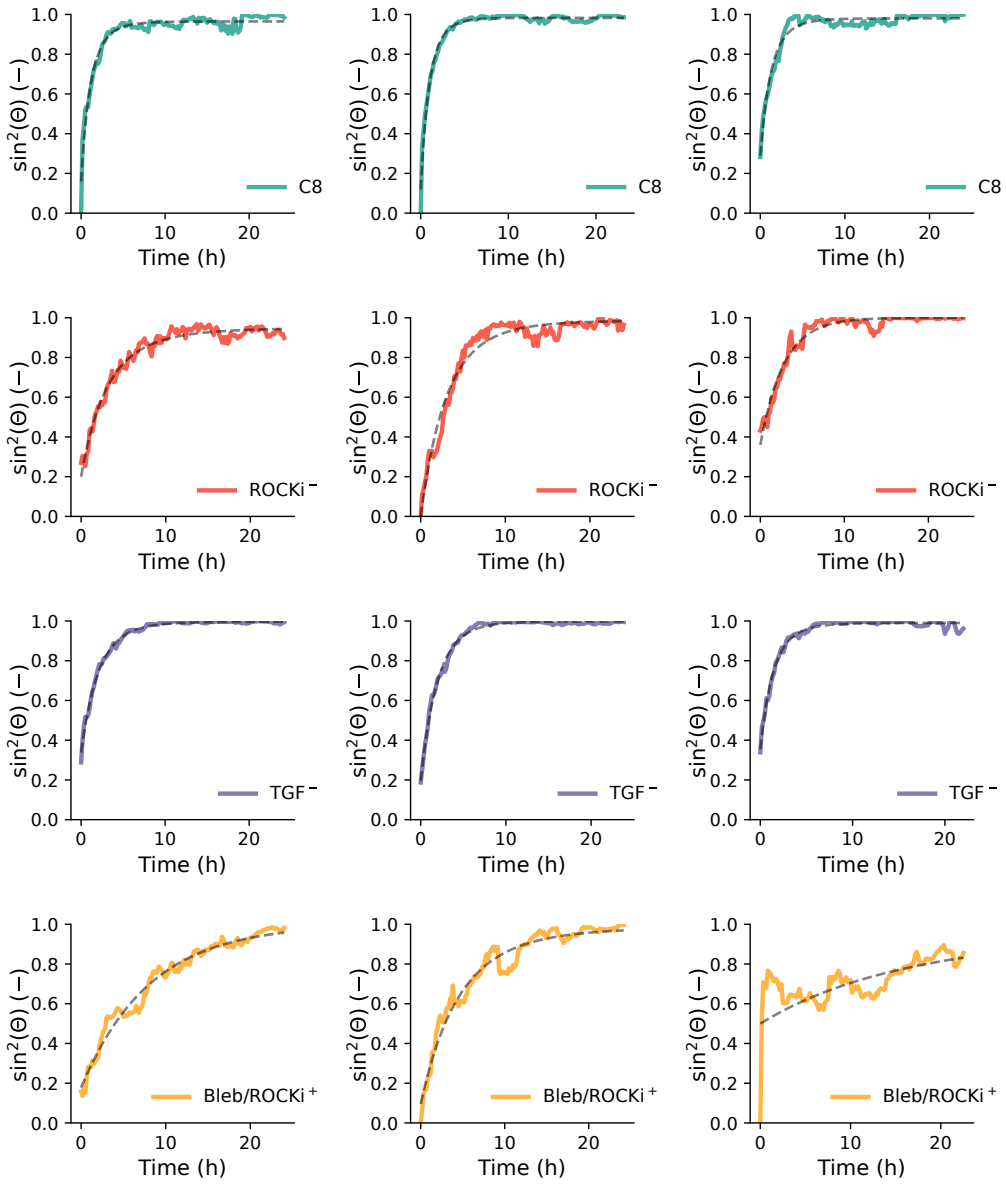

Supplementary Fig. 3: Illustration of goodness of fit on single observation of tissue spheroid fusion, as shown by the temporal evolution of the fusion angle for three individual replicas and 4 media compositions, together with the fit of the governing dynamics $2\dot{\theta} = \cot(\theta)/\tau_\Gamma - \sin(\theta)/\tau_\varepsilon$. Representative samples are shown. The total sample count (n) is provided in Supplementary Fig. 2.

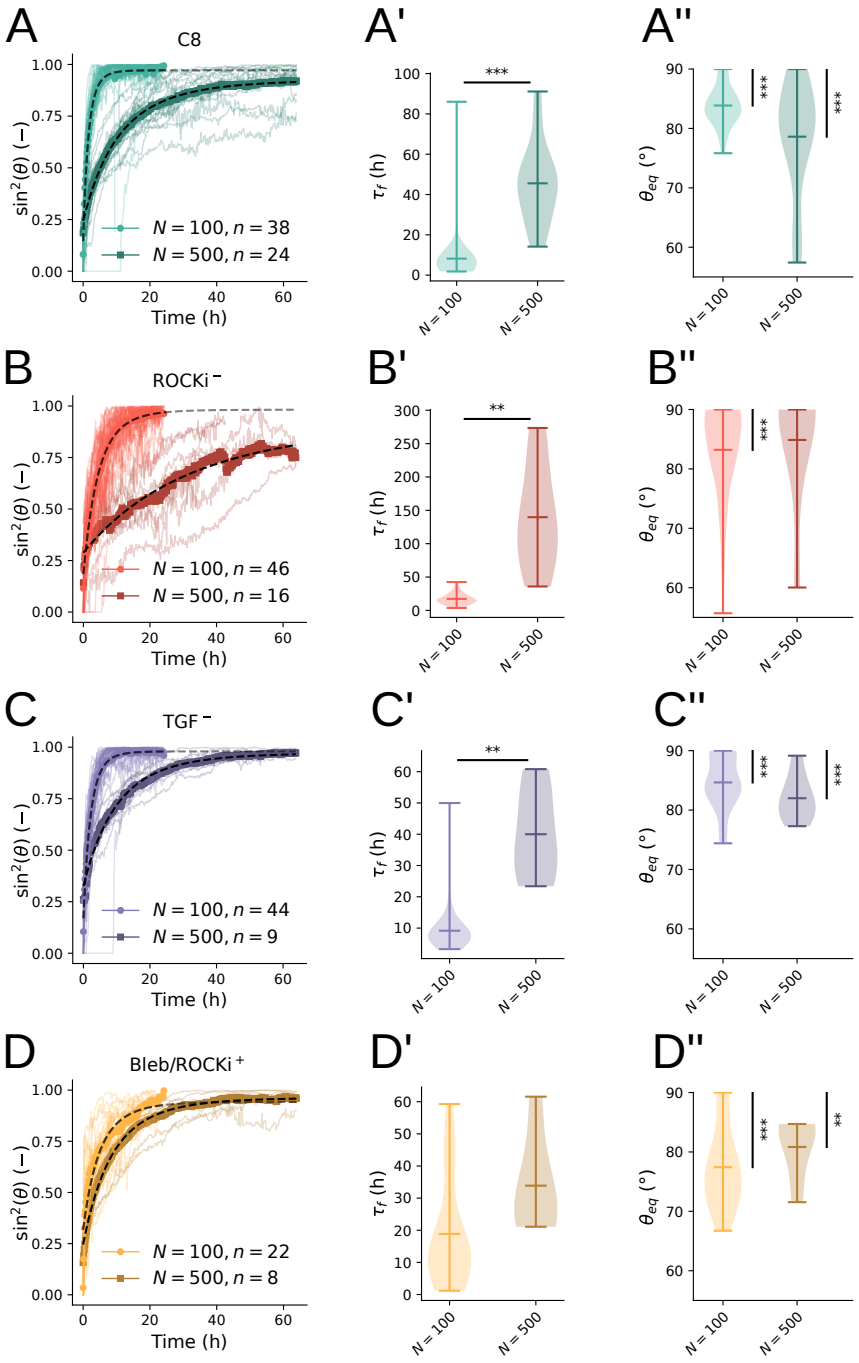

Supplementary Fig. 4: **Visco-elastic fusion dynamics of small and large tissue spheroids. A-D**: Temporal evolution of the angle during fusion of small $N = 100$ and larger $N = 500$ spheroids in conditions C8, ROCKi$^-$, TGF$^-$ and Bleb/ROCKi$^+$. Light curves are individual repeats and markers indicate the average fusion dynamics. The dashed line is the fit of Eq. 1. **A'-D'**: Estimated fusion timescale τ_f for 5 conditions, indicating significant differences between small and large aggregates (two-sided Welch's t-test, $p > 0.05$ * $p > 0.01$ ** $p > 0.001$ ***, with $p = 3.60\text{E-}7$ (C8), 0.0036 (ROCKi$^-$), 0.0011 (TGF$^-$), 0.075 (Bleb/ROCKi$^+$)); and **A''-D''**: Equilibrium fusion angle θ_{eq}, indicating significantly different fusion angles from 90° (one-sided t-test, $p > 0.05$ * $p > 0.01$ ** $p > 0.001$ ***, with $p = 1.45\text{E-}13$ (C8, $N = 100$), 9.08E-5 (C8, $N = 500$), 3.95E-7 (ROCKi$^-$, $N = 100$), 0.11 (ROCKi$^-$, $N = 500$), 1.98E-9 (TGF$^-$, $N = 100$), 8.96E-4 (TGF$^-$, $N = 500$), 3.77E-7 (Bleb/ROCKi$^+$, $N = 100$), 4.02E-3 (Bleb/ROCKi$^+$, $N = 500$)). Data are pooled from independent biological repeats (5 for $N = 100$, see Supplementary Fig. 2, and 1 for $N = 500$); sample numbers (n) are indicated in panels A–D. Horizontal bars represent the mean and data extrema (min–max).

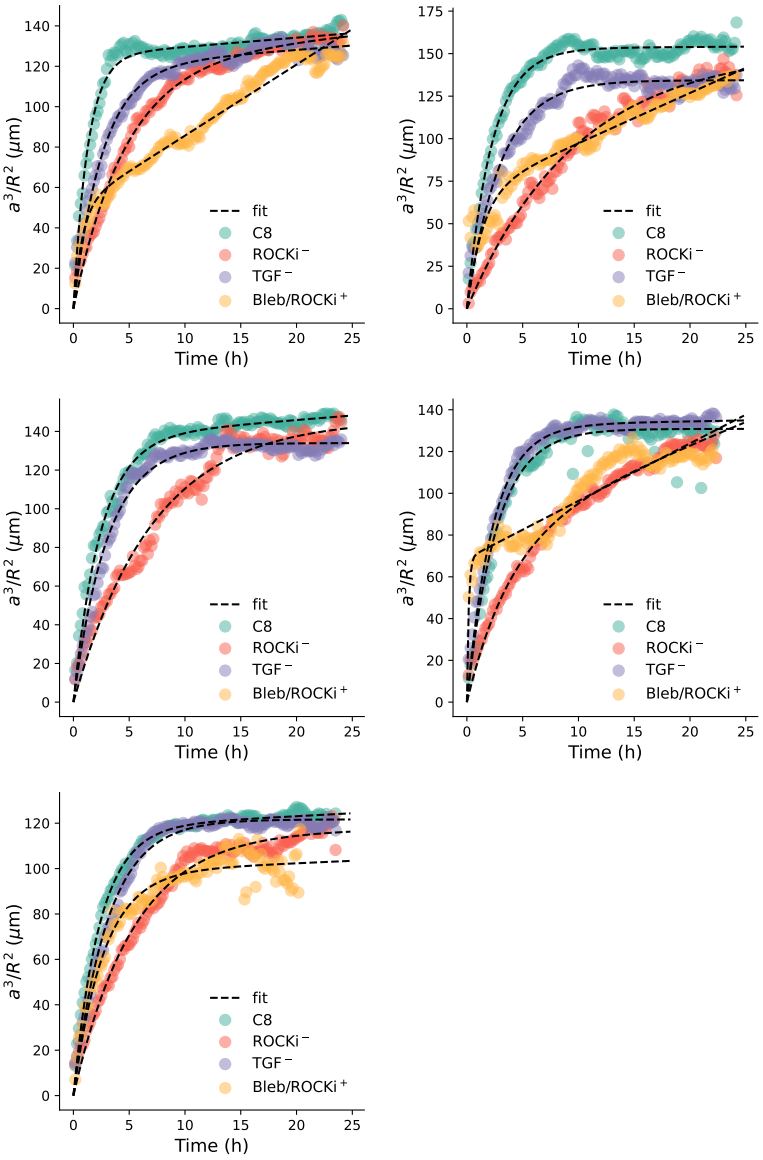

Supplementary Fig. 5: Alternative fit of fusion data for 4 media compositions, based on the model of Beaune et al. for viscoelastic liquid fusion. This model predicts governing dynamics as $a^3/R^2 \approx L_e(1-e^{-t/\tau_1})+v_f t$, with contact radius a, aggregate radius R, elastic length-scale L_e, (initial) visco-elastic relaxation time τ_1 and fusion velocity v_f. Individual fits are shown by dashed lines. Total sample count n is indicated in Supplementary Fig. 2.

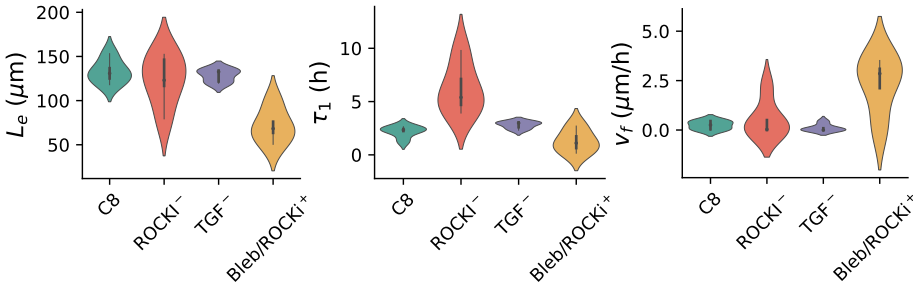

Supplementary Fig. 6: Fit values of data shown in Supplementary Fig. 5 for parameters L_e (elastic length-scale), τ_1 (initial visco-elastic relaxation time) and v_f (effective fusion velocity), for 4 studied medium compositions. Total sample count n is indicated in Supplementary Fig. 2.

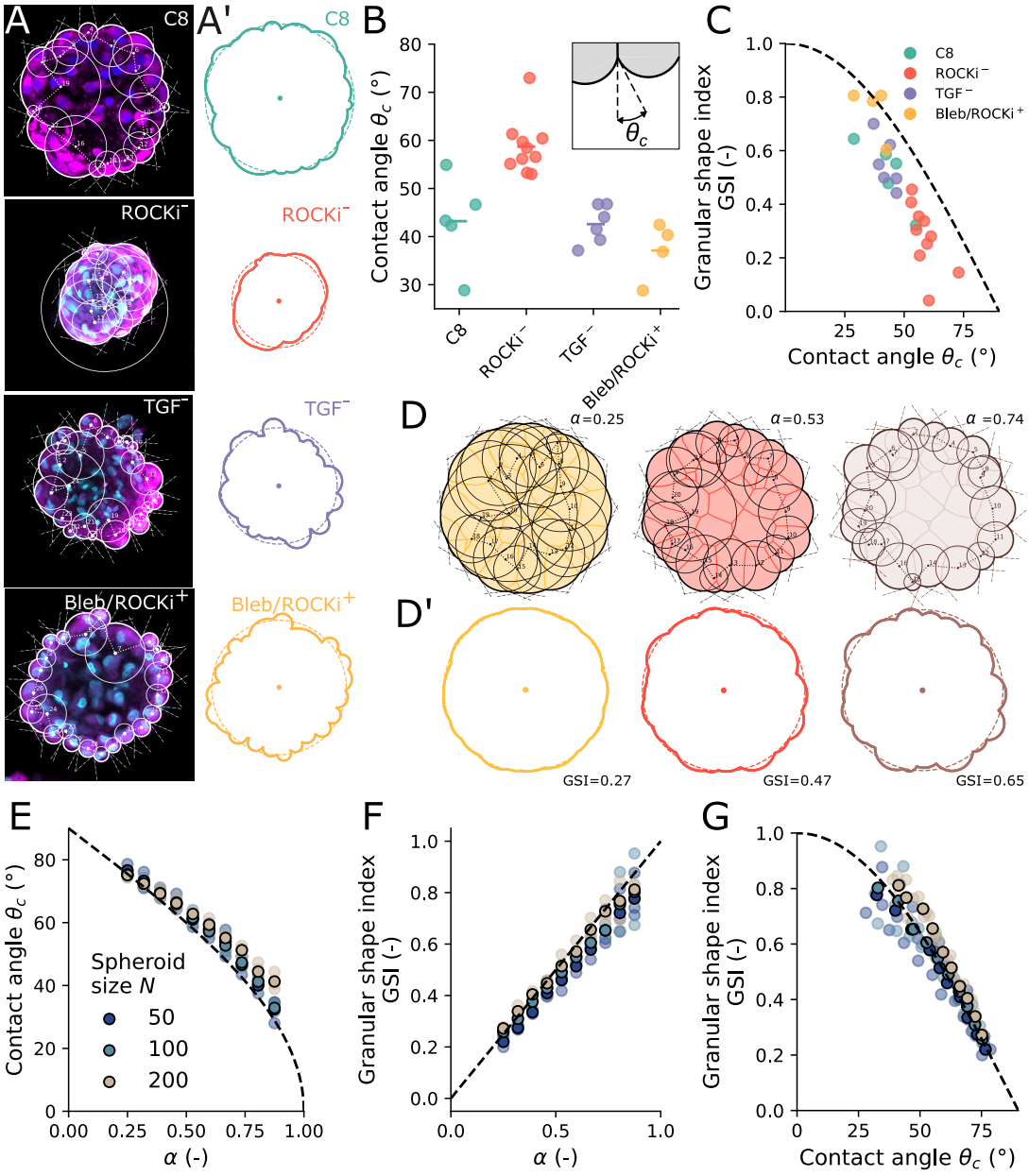

Supplementary Fig. 7: **Granular shape index is a measure of relative cell-cell tension.** **A**: Confocal microscopy slices of representative spheroids in conditions C8, ROCKi^{-}, TGF^{-} and Bleb/ROCKi^{+}, with DAPI staining (nucleus), annotated with fitted contour circles, and **A'**, extracted spheroid contour with fitted spheroid radius. Representative samples are shown. The total number of samples with successful contour fits was $n = 5$ (C8), $n = 10$ (ROCKi^{-}), $n = 6$ (TGF^{-}), and $n = 4$ (Bleb/ROCKi^{+}). **B**: Extracted contact angle θ_c (inset) in 4 conditions, based on the contact angle between individual cells at the aggregate contour. Each data point represents the median contact angle from a single spheroid, with the horizontal bar indicating the average across n spheroids in each condition. Measurements are biased towards lower contact angles due to difficulties in distinguishing contacts between neighboring cells with low curvature (compare a and d) and the presence of bleb-like protrusions in otherwise smooth aggregates. **C**: Granular shape index (GSI) in function of extracted contact, with theoretical scaling $GSI = \cos(\theta_c)$ as a dashed line. **D**: Slices of simulated tissue spheroids at varying α, annotated with fitted contour circles, and **D'**, extracted spheroid contour with fitted spheroid radius, annotated with the corresponding GSI. **E**: In simulated spheroids of varying size N, where θ_c can be accurately determined, contact angle measures relative cell-cell tension α. The dashed line shows $\theta_c = \arccos(\alpha)$. **F**: Granular shape index measures α in simulated tissue spheroids. The dashed line shows $GSI = \alpha$. **G**: GSI closely follows the theoretical scaling, $GSI = \cos(\theta_c)$, in simulated tissue spheroids.

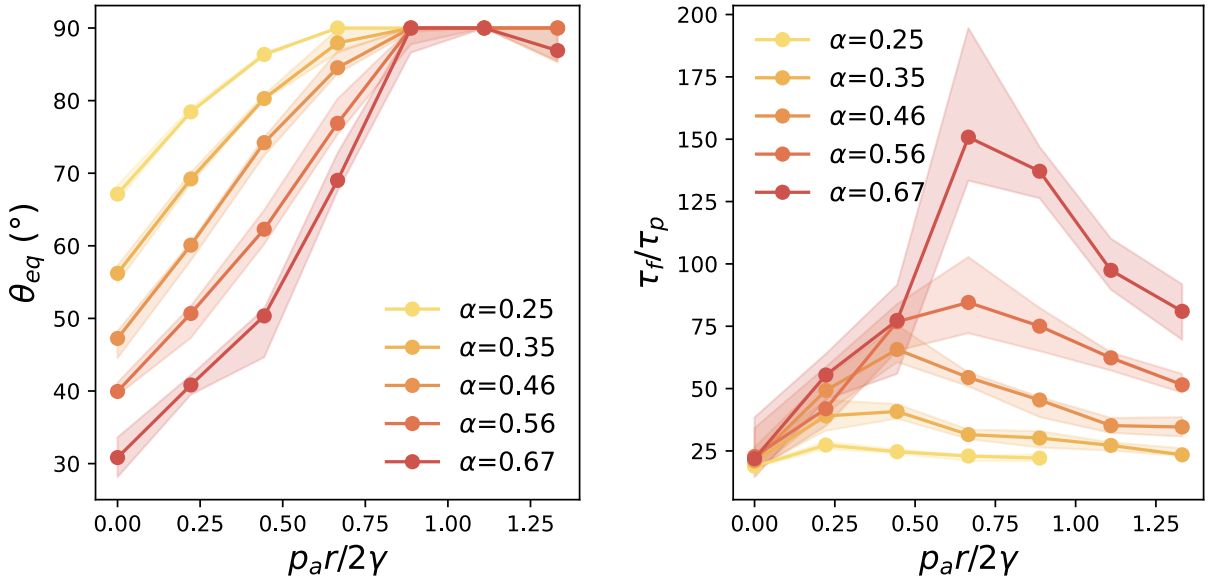

Supplementary Fig. 8: Fusion angle θ_{eq} (left) and fusion time τ_f (right) versus active pressure $p_a r/(2\gamma)$, at varying relative tension α, from active foam simulations. Circles and solid lines show medians; shaded regions denote interquartile ranges across 10 random repeats. This panel presents the data distribution underlying Fig. 3F–G, where each pixel represents the mean per parameter set. Top two rows from Fig. 3F–G (highly granular regimes with large τ_f fluctuations) are excluded for clarity.

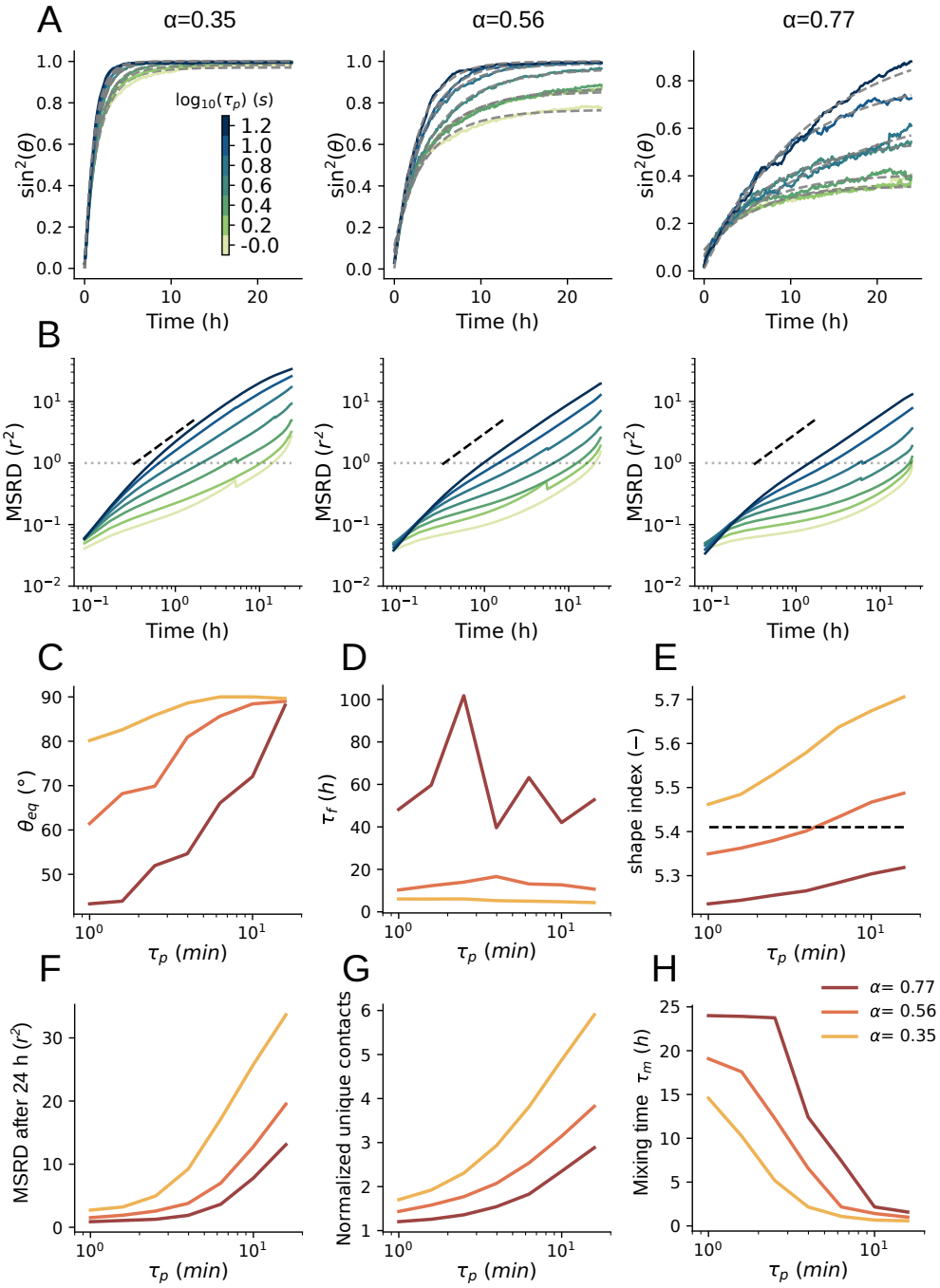

Supplementary Fig. 9: **Persistence time affects fusion dynamics and tissue fluidity.** **A**: Fusion angle in function of time for simulated spheroids with varying persistence time τ_p, at three levels of relative cell-cell tension α. Decreased τ_p leads to incomplete fusion. Fitted curves of Eq. 1 are shown with fitted parameters in c,d. **B**: Mean squared relative displacement (MSRD) in function of time for varying τ_p and α, with horizontal dashed line indicating $MSRD = r^2$ and black dashed line indicating diffusive scaling. Decreasing τ_p induces jamming. **C**: Equilibrium fusion angle θ_{eq} increases with τ_p. **D**: τ_p has no pronounced effect on fusion time τ_f. **E**: Shape index increases with τ_p, indicating larger cell deformations and tissue fluidization. The dashed line indicates prediction of a critical shape index at 5.41 from 3D vertex models. **F**: MSRD after 24 h increases with τ_p. **G**: Normalized unique contacts, indicating frequency of cell rearrangements, increases with τ_p. Note the similarities between f and g. **H**: Microscopic mixing time, defined as the lag-time for which $MSRD = r^2$ and capped at 24h, decreases with τ_p. All reported data shows the average across 10 random repeats.

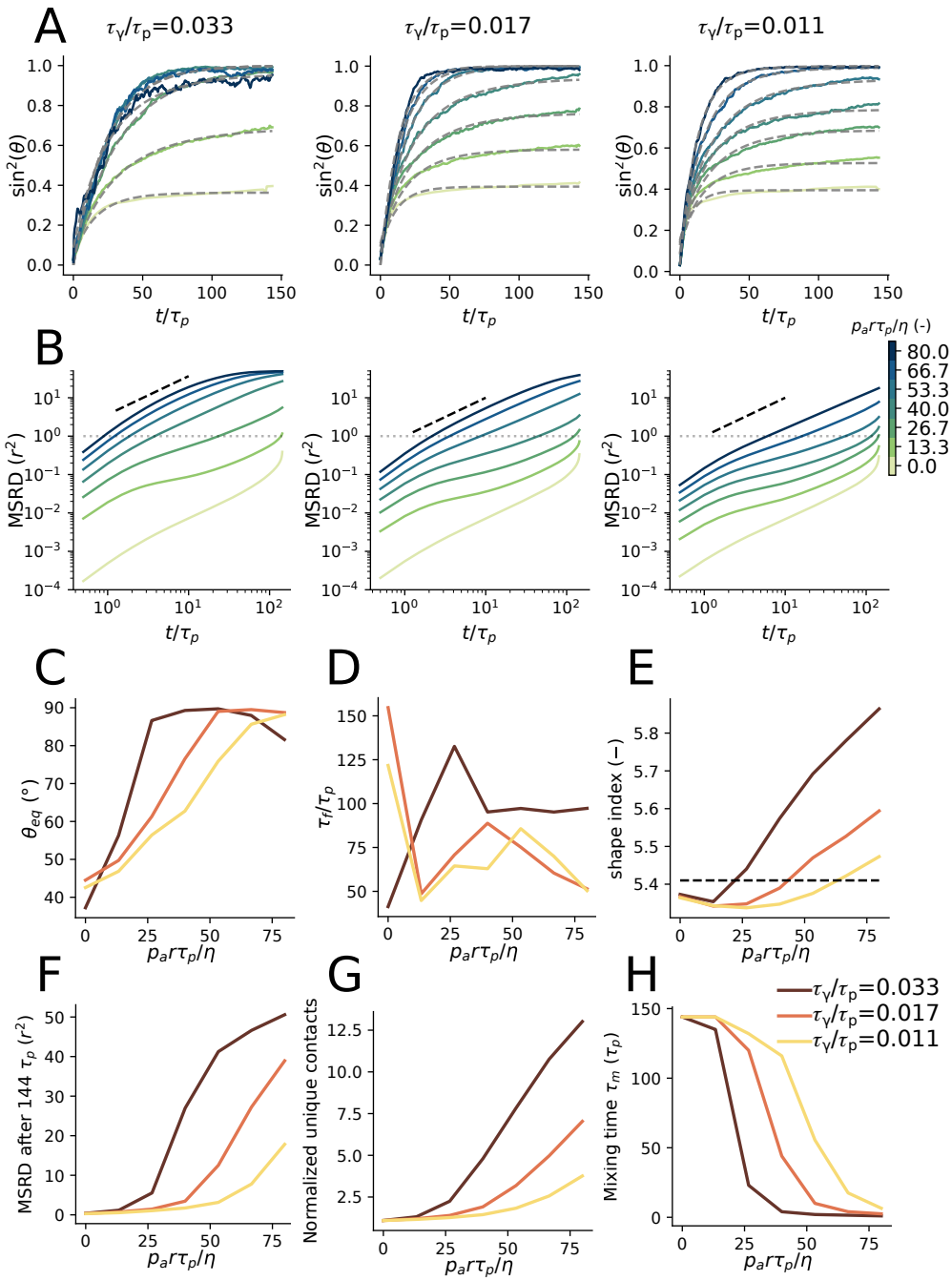

Supplementary Fig. 10: **Surface tension affects fusion dynamics by promoting jamming.** **A**: Fusion angle in function of time for simulated spheroids with varying rescaled motility $p_a r\tau_p/\eta$ at three levels of surface tension (cortex tension at the cell-medium interface), parameterized by cortical relaxation time $\tau_\gamma = \eta/\gamma$. Decreased τ_γ leads to incomplete fusion. Fitted curves of Eq. 1 are shown with fitted parameters in c,d. **B**: Mean squared relative displacement (MSRD) in function of time for varying τ_γ/τ_p and $p_a r\tau_p/\eta$, with horizontal dashed line indicating $MSRD = r^2$ and black dashed line indicating diffusive scaling. Decreasing τ_γ/τ_p reduces relative displacements. **C**: Equilibrium fusion angle θ_{eq} increases with τ_γ/τ_p. **D**: Fusion time τ_f/τ_p decreases with τ_γ/τ_p at low cell motility, but increases at high cell motility. **E**: Shape index increases with τ_γ/τ_p, indicating larger cell deformations and tissue fluidization. The dashed line indicates prediction of a critical shape index at 5.41 from 3D vertex models. **F**: MSRD after 144 τ_p increases with τ_γ/τ_p. **G**: Normalized unique contacts, indicating frequency of cell rearrangements, increases with τ_γ/τ_p. Note the similarities between f and g. **H**: Microscopic mixing time, defined as the lag-time for which $MSRD = r^2$ and capped at 144 τ_p, decreases with τ_γ/τ_p. All reported data shows the average across 10 random repeats.

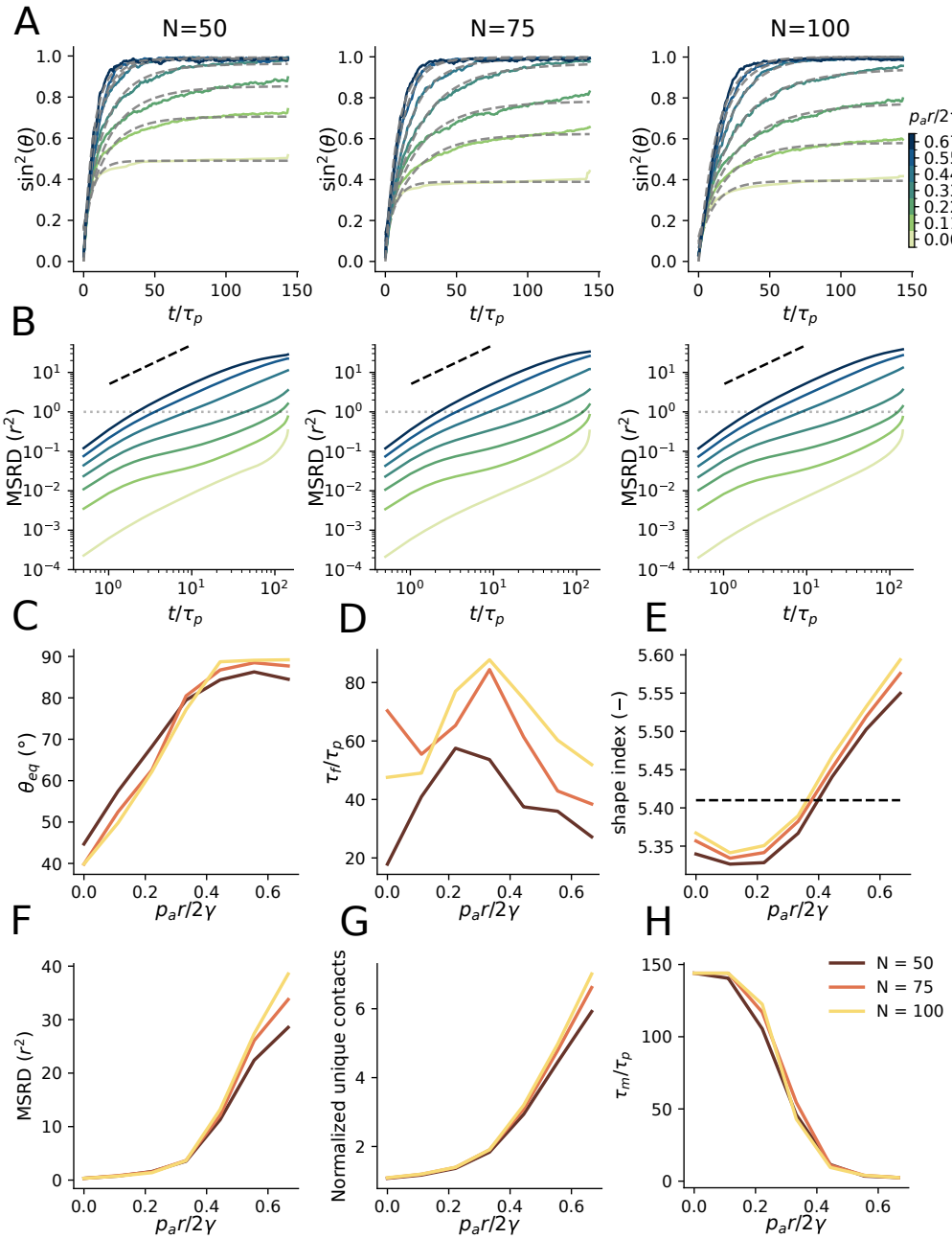

Supplementary Fig. 11: **Weak size effects on fusion dynamics and tissue fluidity for small spheroids.** **A**: Fusion angle in function of time for simulated spheroids with varying motility $p_a r/2\gamma$, at three spheroid sizes, with number of cells $N = 50, 75, 100$. Increased size weakly favors incomplete fusion. **B**: Mean squared relative displacement (MSRD) in function of time for varying N and $p_a r/2\gamma$, with horizontal dashed line indicating $MSRD = r^2$ and black dashed line indicating diffusive scaling. There is no pronounced effect of spheroid size on relative displacements. **C**: At low motility, smaller spheroids show more complete fusion. At high motility, decreased spheroid size leads to $\theta_{eq} < 90°$, as active surface fluctuations are more pronounced at small N. In the studied range of spheroid sizes, these effects are weak. **D**: Fusion time increases with spheroid size. **E**: Shape index, indicating cell deformations, weakly increases with spheroid size. The dashed line indicates prediction of a critical shape index at 5.41 from 3D vertex models. **F**: No pronounced effect of spheroid size on the MSRD after 144 τ_p. **G**: Normalized unique contacts, indicating frequency of cell rearrangements, do not strongly depend on spheroid size. **H**: Microscopic mixing time, defined as the lag-time for which $MSRD = r^2$ and capped at 144 τ_p, does not depend on spheroid size. All reported data shows the average across 10 random repeats.

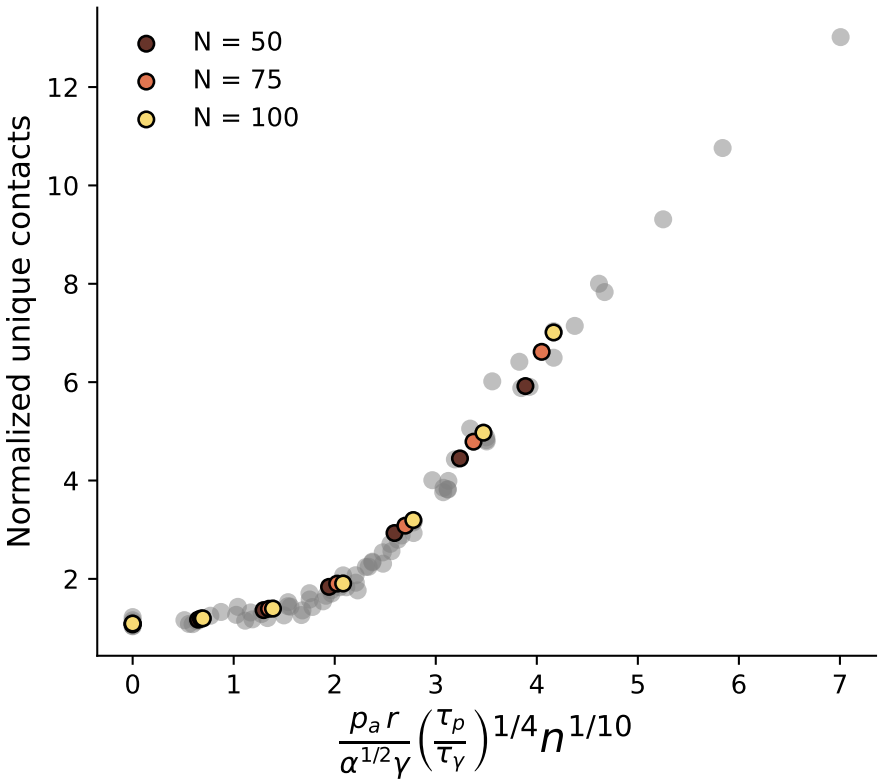

Supplementary Fig. 12: Normalized unique contacts for varying p_a, τ_p, and α (background), as well as number of cells N (marker color). A weak scaling (approximately $\propto N^{1/10}$) with cell number can be observed (Extension of Fig. 4E).

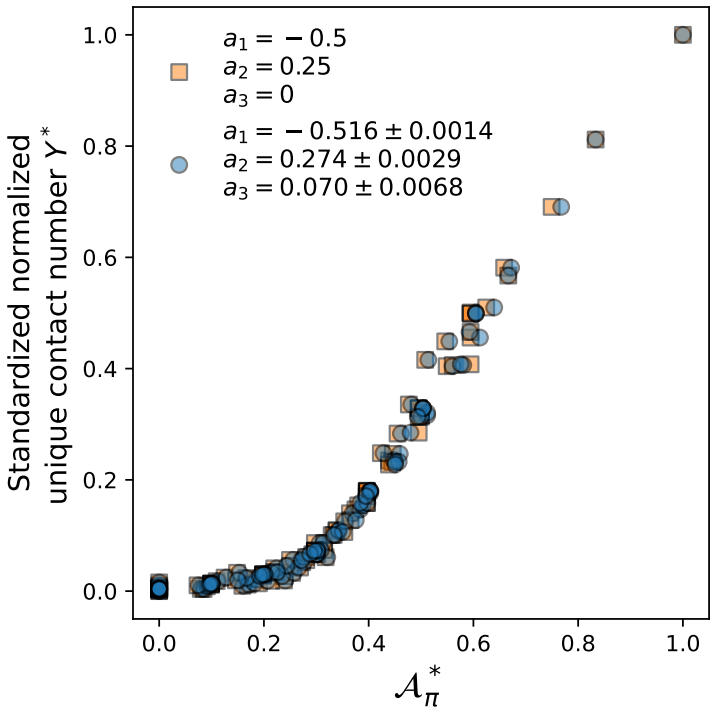

Supplementary Fig. 13: Standardized normalized unique contacts Y^* in function of standardized dimensionless activity $\mathscr{A}_\pi^*$, with $\mathscr{A}_\pi = (p_a r/\gamma)^1 (\alpha)^{a_1} (\tau_p/\tau_\gamma)^{a_2} N^{a_3}$ (see methods), showing theoretical scaling with exponents $a_1 = -1/2, a_2 = 1/4$ and $a_3 \approx 0$, and estimated exponents that optimize rank and smoothness of Y^* in function of $\mathscr{A}_\pi$.

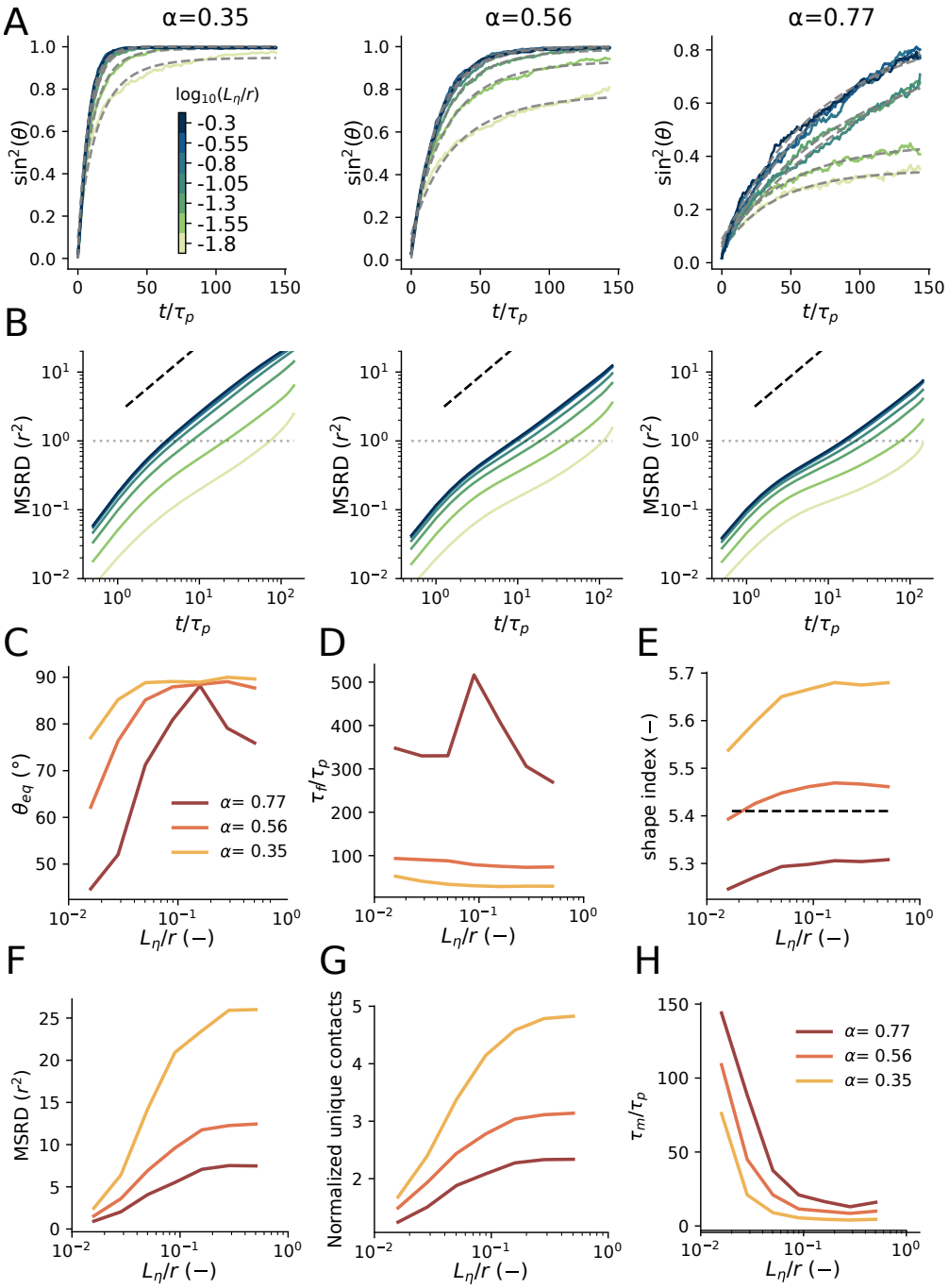

Supplementary Fig. 14: **Cell-cell friction induces arrested fusion** **A**: Fusion angle in function of time for simulated spheroids with varying cell-cell friction, at three levels of relative cell-cell tension α. Friction is parameterized through the hydrodynamic length-scale $L_\eta = (\eta/\xi)^{1/2}$, with cortex viscosity η and cell-cell friction constant ξ (High values of L_η correspond to low cell-cell friction). Cell-cell friction induces arrested fusion. **B**: Mean squared relative displacement (MSRD) in function of time for varying L_η and α, with horizontal dashed line indicating $MSRD = r^2$ and black dashed line indicating diffusive scaling. Cell-cell friction decreases MSRD and promotes jamming. **C**: Cell-cell friction leads to incomplete fusion. At low friction and large α, the spheroid is an agitated granular pile with equilibrium fusion angle $\theta_{eq} < 90°$. **D**: Cell-cell friction weakly increases relative fusion time τ_f/τ_p. **E**: Shape index weakly decreases with cell-cell friction. At high friction and low cell-cell tension, jamming (see f,g), is induced for elongated cells (shape index > 5.41), indicating that jamming induced by cell-cell friction is a distinct mechanism from shape driven rigidity transitions. The dashed line indicates prediction of a critical shape index at 5.41 from 3D vertex models. **F**: Cell-cell friction sharply decreases the MSRD after 144 τ_p. **G**: Normalized unique contacts, indicating frequency of cell rearrangements, sharply decrease with increased cell-cell friction **H**: Mixing is strongly reduced by increasing cell-cell friction, as indicated by the microscopic mixing time, defined as the lag-time for which $MSRD = r^2$ (capped at 144 τ_p). All reported data shows the average across 10 random repeats.

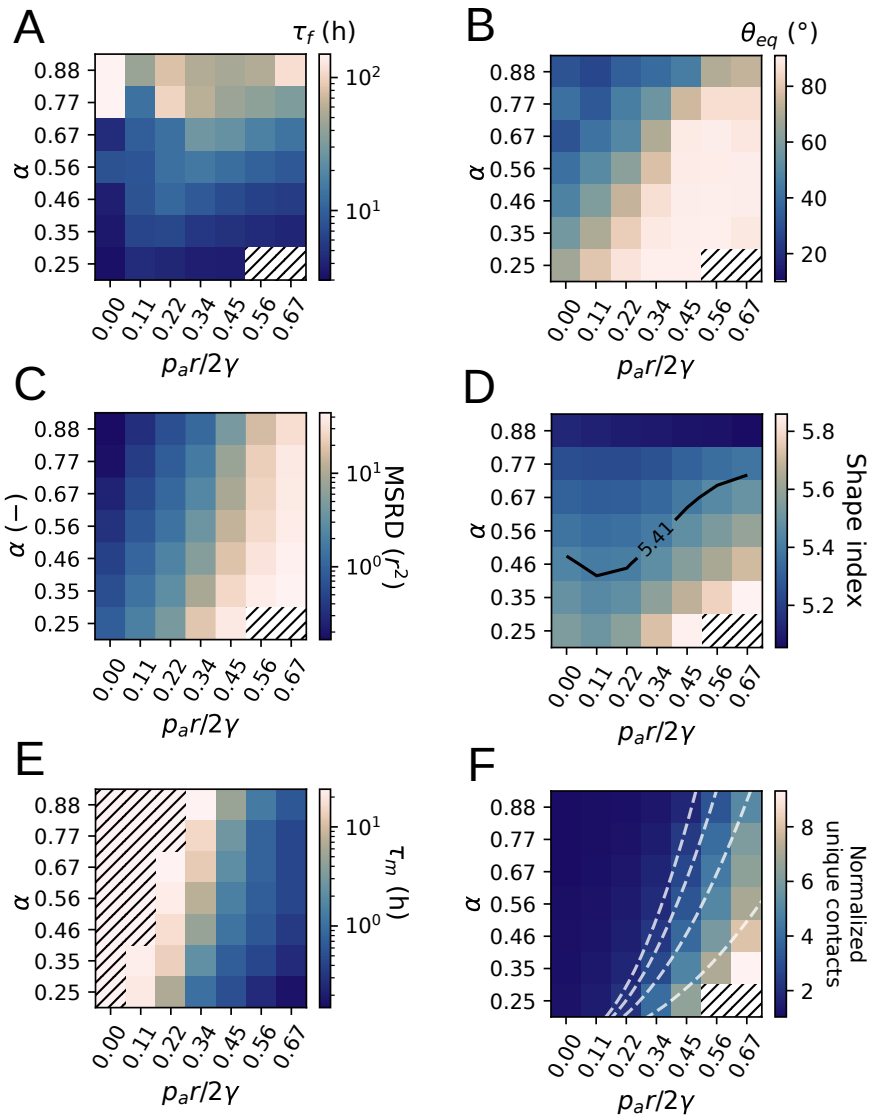

Supplementary Fig. 15: Detailed overview of the effect of active protusion pressure p_a and relative cell-cell tension α on fusion dynamics and cell motility. **A)** Fusion time-scale τ_f. **B)** Equilibrium fusion angle θ_{eq}. **C)** Mean squared relative displacement (MSRD) after 24 hours of fusion. **D)** Shape index at the end of fusion. 3D vertex models predict a transition form jammed to fluidized at around 5.41, which is shown by the black dashed line. **E)** Microscopic mixing time which is defined as the lag-time for $MSRD = r^2$. Here, the zone hatched indicates the parameter region where this threshold was not reached at the end of the 24 hour simulation. **F)** Normalized unique contacts after 24 hours of fusion. Dashed lines show the scaling $\alpha \propto (p_a r/2\gamma)^2$. Hatched data points in (a, b, c, d, f) show simulations that failed to converge at high motility and low α. All reported data shows the average across 10 random repeats.